JOURNAL OF MAGNETIC RESONANCE **124,** 420–438 (1997)
ARTICLE NO. MN961052

Four-Dimensional ^{1}H and ^{23}Na Imaging Using Continuously Oscillating Gradients

J. M. STAR-LACK,* M. S. ROOS, S. T. S. WONG, V. D. SCHEPKIN, AND T. F. BUDINGER

Center for Functional Imaging, Lawrence Berkeley National Laboratory, 1 Cyclotron Road, MS 55-121, Berkeley, California 94720

Received July 15, 1996; revised October 28, 1996

A class of fast magnetic spectroscopic imaging methods using continuously oscillating gradients for four-dimensional (three spatial and one spectral) localization is introduced. Sampling may start immediately following the application of an RF excitation pulse, thus enabling measurement of spin density, chemical shift, and relaxation rates of short-T_2 species. For spatial localization, steady-state sinusoidal gradient waveforms are used to sample a ball in k space. The two types of trajectories presented include: (1) continuously oscillating gradients with continuously rotating direction used for steady-state free-precession imaging and (2) continuously oscillating gradients followed by a spoiler directed along discrete projections. Design criteria are given and spatial–spectral and spatial–temporal reconstruction methods are developed. Theoretical point-spread functions and signal-to-noise ratios are derived while considering T_2^*, off-resonance effects, and RF excitation options. Experimental phantom, *in vivo,* and *in vitro* ^{1}H and ^{23}Na images collected at 2.35 T are presented. The ^{1}H images were acquired with isotropic spatial resolution ranging from 0.03 to 0.27 cm^3 and gradient-oscillation frequencies ranging from 600 to 700 Hz, thus allowing for the separation of water and lipid signals within a voxel. The ^{23}Na images, acquired with 500 and 800 Hz gradient waveforms and 0.70 cm^3 isotropic resolution, were resolved in the time domain, yielding spatially localized FIDs.

INTRODUCTION

Magnetic resonance spectroscopic imaging (MRSI) using continuously oscillating sinusoidal B_0 gradient waveforms with deterministic RF excitation was first proposed by Macovski (*1*), who showed that both spectral and spatial information may be encoded simultaneously. Compared with conventional trapezoidal pulses, a steady-state sinusoidal waveform can reduce gradient-amplifier requirements while ameliorating some of the deleterious effects of induced B_0 eddy currents. Sampling may commence immediately following RF excitation, thus permitting visibility of short-T_2 species. In addition, signal enhancement may be achieved by utilizing steady-state free-precession effects. Several theoretical papers (*2–6*) treated reconstruction with a variety of continuously oscillating gradient trajectories. Previous experimental work includes a 1D water-phantom study (*7*) and 2D phantom studies of solids (*8, 9*). In these previous studies, neither chemical shift nor T_2^* was spatially localized.

This paper introduces a class of four-dimensional (three spatial and one spectral) rapid imaging schemes using periodic short-duration RF pulses with continuously oscillating gradients to sample a solid sphere in k space. Reconstruction methods are developed and the theoretical point-spread functions (PSFs) and signal-to-noise ratios (SNRs) are derived. In addition, experimental phantom, *in vitro*, and *in vivo* ^{1}H and ^{23}Na data spatially localizing T_2^* or chemical shift are presented. The ability to quantify the ^{23}Na biexponential decay process may lead to the estimation of relative intra- and extracellular ion concentrations and be of important diagnostic potential (*10–16*). Short-T_2 proton spectroscopic imaging which differentiates water and lipid signals may be useful in characterizing a wide range of processes, including arteriosclerosis, and bone and joint diseases (*17, 18*).

Two different gradient paths are presented. Figure 1a shows GR_{ss}—a steady-state free-precession (SSFP) sequence consisting of continuously oscillating/rotating gradients. Figure 1b shows GR_{sp}—a spoiled sequence comprising a sinusoidal gradient waveform directed along discrete projections followed by a crusher. The (k, t)-space trajectories are similar to those of the projection-reconstruction echo-planar experiment (PREP) (*19*) since, after excitation, the sampling trajectory oscillates between the k-space origin and a maximum radius k_{max}.

For GR_{ss}, the gradient waveforms are in near steady state as the frequency of rotation is much slower than the frequency of oscillation. With GR_{sp}, each sinusoidal projection-gradient waveform is first turned on for a warm-up period to allow a steady state to be reached before excitation and sampling. One advantage of using a steady-state gradient waveform is that the B_0 eddy currents will also be in near steady state, thus causing more predictable spin dephasing than eddy currents produced by pulsed waveforms. Our ex-

* To whom correspondence should be addressed at Department of Radiology, MC5488, Stanford University, Stanford, California 94305.

1090-7807/97 $25.00

perimental experience indicates that the only correction required with steady-state gradients is to properly calibrate the phase of the programmed waveform to account for linear phase delays that may be caused by amplifier hardware and eddy currents. This aspect is further discussed under Experimental Methods.

Two different excitation options are introduced, which are shown in Fig. 2: (2a) RFa, excitation at the gradient maximum; and (2b) RFb, excitation at (or slightly before) a gradient zero. An advantage of RFa is that both sides of the *k*-space origin are sampled after each excitation. However, since there is no slice selection, peak RF power requirements may be higher for RFa as the bandwidth of the excitation pulse must be sufficient to excite the entire sample. Comparatively, the RFb excitation pulse may be of narrower bandwidth and commence slightly before the gradient zero to allow sampling of the origin of *k* space after probe ringdown. In further examining the RFa and RFb excitation schemes, other issues which will be addressed include their respective point-spread functions and signal-to-noise ratios, while considering the effects of chemical shift, B_0 inhomogeneities, and T_2 decay.

The paper first presents the methodology of the techniques including the *k*-trajectory and excitation options. Next, reconstruction procedures are described and point-spread functions and SNRs are derived and evaluated. The theoretical steady-state magnetization vectors resulting from the different trajectories (GR_{ss} and GR_{sp}) are then analyzed. Finally, experimental ^{1}H and ^{23}Na phantom, *in vitro*, and *in vivo* results are presented.

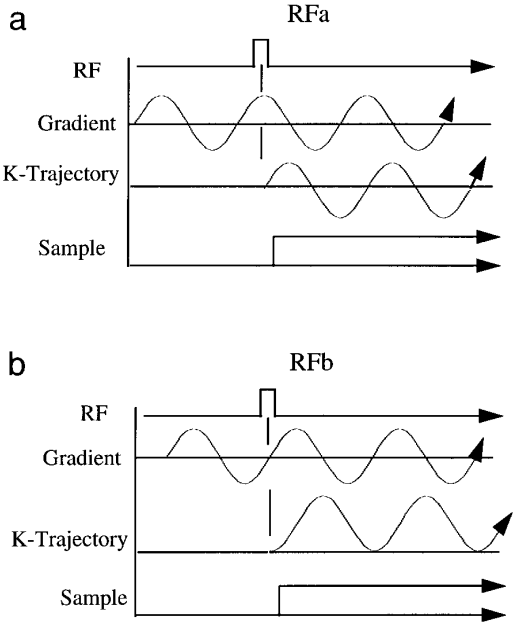

FIG. 2. Two alternative excitation options. (a) RFa—excitation at the gradient waveform maximum. The *k* trajectory spans both sides of the *k*-space origin. (b) RFb—excitation at a waveform zero. The RF pulse may be placed slightly before the gradient zero to allow for probe ringdown to occur before sampling the *k*-space origin.

THEORY

The following subsections describe and analyze: (1) *k*-space trajectories, gradient waveforms, and excitation options; (2) reconstruction techniques and the resulting point-spread functions while considering T_2^* and chemical shift; (3) reconstruction noise; and (4) steady-state magnetization and contrast mechanisms.

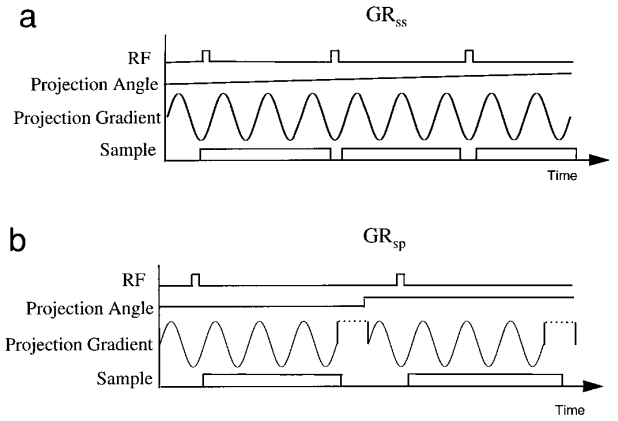

FIG. 1. Two alternative gradient trajectories. (a) GR_{ss}—continuously oscillating/rotating gradients; and (b) GR_{sp}—continuously oscillating gradients with discrete projections.

k-Space Trajectories and Gradient Waveforms

Four different possible *k*-space trajectories exist since each of the two excitation schemes (RFa, RFb) may be combined with one of two gradient paths (GR_{sp}, GR_{ss}). For all gradient and RF combinations, the *k* trajectory oscillates between the *k*-space origin and a maximum radius k_{max}, while the projection angle changes either discretely (GR_{sp}) or continuously (GR_{ss}) in time. Thus, for a full *k*-space scan, the acquired *k*-space volume comprises concentric spheres centered about and including $k = 0$. To ensure that the sampling density is spherically symmetric, the projection directions are calculated from a sample path designed to cover the surface of a sphere uniformly (*20*). The sample path starts at the top pole and spirals downward as shown in Fig. 3.

The equations for the continuously oscillating rotating *k* trajectory (GR_{ss}) are

GR_{ss}:

$$k_x(t) = k_r(t)\cos\{\sqrt{\zeta}\sin^{-1}[z'(t)]\}\sqrt{1 - [z'(t)]^2},$$
$$k_y(t) = k_r(t)\sin\{\sqrt{\zeta}\sin^{-1}[z'(t)]\}\sqrt{1 - [z'(t)]^2},$$
$$k_z(t) = k_r(t)z', \quad 0 \leq t \leq T_{exp}, \qquad [1]$$

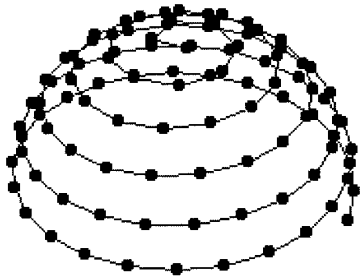

FIG. 3. The uniform sampling trajectory on the top half of the unit sphere generated with Eq. [1]. Superimposed are the discretely sampled points used to compute the projection angles for the GR_{sp} sequence.

where $k_r(t)$ is the time-dependent radial k-space position, $z'(t) = 1 - 2t/T_{exp}$ is the z-axis position of the trajectory within the unit circle, and $\zeta = \pi N_{rf}$ is the rotational frequency coefficient. The experiment time T_{exp} is the product of the number of RF excitations N_{rf} and the pulse repetition time T_R. The RF excitation pulses are applied at times $t_p = pT_R$, where the pulse index $p = 0, 1, \ldots, N_{rf} - 1$.

To avoid spatial aliasing, the distribution of the sample points at all k-space radii must be sufficiently dense to characterize spatial frequencies over the entire image field of view (FOV). Since there is no slice selection, the FOV should be at least equal to the maximum sample diameter. To meet this Nyquist-sampling requirement, N_{rf} needs to be large enough so that the angular spacing between sample points at the k-space radius k_{max} is less than or equal to $1/\mathrm{FOV}$. Thus, the minimum number of excitations can be calculated from the surface area of the k-space sampling sphere ($4\pi k_{max}^2$) and the FOV and, for a full k-space scan (projections spanning a solid angle 4π), is

$$N_{rf} \geq (\sqrt{3}/2)(4\pi \mathrm{FOV}^2 k_{max}^2). \quad [2]$$

The factor $(\sqrt{3}/2)$ arises from the approximate hexagonal sampling distribution provided by the trajectory. Note that while Eq. [2] gives the advised minimum number of excitations (projections) to sample a spherical FOV unaliased, it is often possible in practice to reduce N_{rf} with only a small reduction in image quality (*21*).

The radial time-dependent k-space position $k_r(t)$ and projection-gradient value $G_r(t)$ for RFa and RFb are
RFa:

$$k_r(t) = k_{max}\sin(\Omega_0 t), \quad G_r(t) = \frac{\gamma k_{max}}{\Omega_0}\cos\Omega_0 t, \quad [3]$$

RFb:

$$k_r(t) = k_{max}[1 - \cos(\Omega_0 t)]/2,$$

$$G_r(t) = \frac{\gamma k_{max}}{2\Omega_0}\sin\Omega_0 t. \quad [4]$$

The gradient amplitude G_0 is $G_0 = \gamma k_{max}/\Omega_0$ (for RFa) and $G_0 = \gamma k_{max}/2\Omega_0$ (for RFb), where γ is the gyromagnetic ratio. The projection-gradient frequency of oscillation (Hz) is $f_0 = \Omega_0/2\pi$.

Both sides of the k-space origin are sampled with each RFa excitation, although twice as much gradient strength is required to attain an equivalent value of k_{max} for a given value of Ω_0. This means that it is possible to still sample a full k-space volume using RFa when z' starts at the pole and stops at the equator. This sequence will be called RFa′ and its use can halve the required minimum number of excitations from that given by Eq. [2]. For the RFa′ trajectory, $z'(t) = 1 - t/T_{exp}$ and $\zeta = 2\pi N_{rf}$.

The projection angles for the continuously oscillating gradient experiment with discrete projections (GR_{sp}) are obtained by setting $k_r(t) = 1$ and sampling Eq. [1] at times $t_p = pT_R$, $p = 0, 1, \ldots, N_{rf} - 1$. Figure 3 shows the continuous trajectory used for GR_{ss} on the top half of the unit sphere as well as superimposed points corresponding to the GR_{sp} projection angles.

Piecewise continuous gradient waveforms may be calculated using first differences to approximate the time derivatives of the k trajectories (Eq. [7]). Care must be taken to ensure that gradient slew rate and magnitude constraints are not violated. Moreover, sample dwell time Δt must be sufficiently short so that the radial spacing between sampled points does not alias the FOV. Assuming a uniform dwell time, if the radial sampling criterion is met at the waveform maximum, it will be met at all times. At the gradient maximum, G_0 aliasing will not occur when

$$\Delta t \leq 1/(\gamma \mathrm{FOV}\, G_0). \quad [5]$$

This constraint also determines the required bandwidth of the RFa excitation pulse.

Reconstruction

Introduction

After the application of an RF pulse p applied at time $t_p = pT_R$, a gradient-echo train is sampled. The Bloch equations yield a signal $s(t)$ given by

$$s(t) = \int_{-\infty}^{\infty}\int_{-\infty}^{\infty} m(\mathbf{r}, \omega) e^{-t'/T_2^*(\mathbf{r},\omega)} e^{i\omega t' - i2\pi \mathbf{r}\cdot\mathbf{k}(t)} d\mathbf{r}\, d\omega, \quad [6]$$

$$\frac{d\mathbf{k}(t)}{dt} = \gamma \mathbf{G}(t). \quad [7]$$

$\mathbf{G}(t)$ and $\mathbf{k}(t)$ are the respective time-dependent B_0 gradient and k-space vectors. The absolute time t is referenced from the beginning of the experiment and determines the k-space position by Eq. [1]. The evolution in k_ω space (the Fourier transform of the spectral domain) is governed by t' which

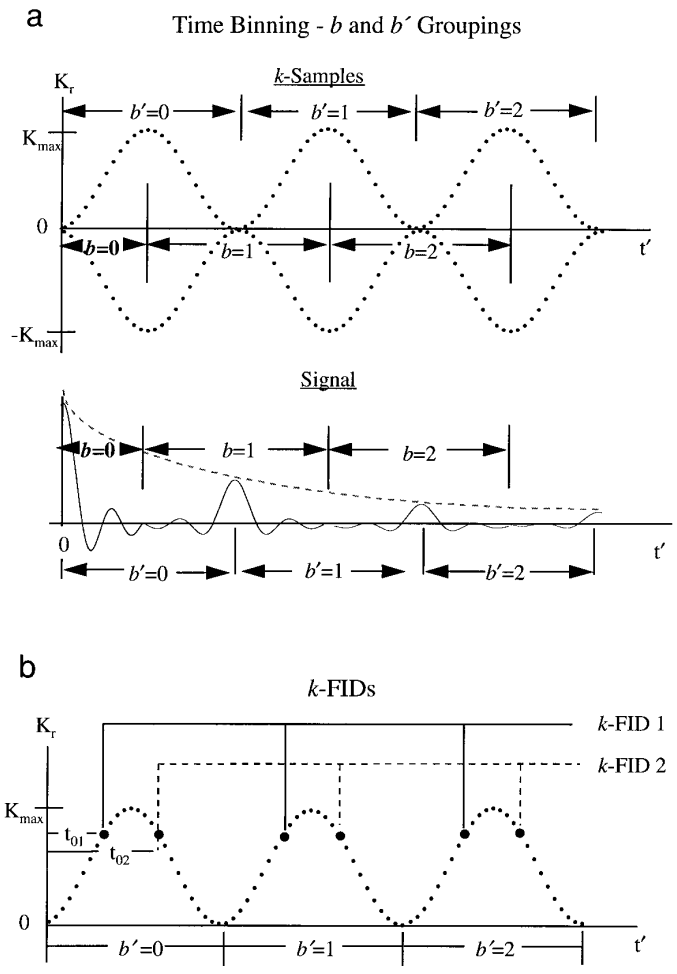

FIG. 4. Grouping of data for reconstruction. (a) The k samples associated with two RFb projections positioned 180° apart are shown. Also shown is a gradient-echo-train signal. For *time binning*, the data sampled during a specific time interval in the echo train are collected together and used to generate a 3D spatial estimate $\hat{m}$. Two alternative groupings are shown—b and b'. Note that the $b = 0$ grouping is unique. For $b > 0$ and $b' \geqslant 0$, each k-space point is sampled twice per bin. (b) k-FIDs—each sampled point in k space is treated as if it is part of a FID with points separated in time by the gradient-oscillation period (for RFb). Note that each unique k-space point has two FIDs with different starting times indicated by t'_{01} and t'_{02} associated with it.

is the time elapsed since the application of the most recent RF pulse p so that $t' = t - t_p$; $m(\mathbf{r}, \omega)$ is the steady-state magnetization density at spatial location $\mathbf{r} = \hat{\mathbf{i}}x + \hat{\mathbf{j}}y + \hat{\mathbf{k}}z$ and chemical shift ω. Any local B_0 inhomogeneities will also be reflected by ω. The nature of the steady-state magnetization $m(\mathbf{r}, \omega)$ resulting from periodic RF pulses is addressed in a later section.

In total, N_{rf} echo trains, each associated with a different projection direction, are sampled. Each echo train comprises N_b gradient echoes b, where $b = 1, 2, \ldots, N_b$. To examine the reconstruction process, we first note that it is possible to collect the sampled data which belong to a specific echo b of each echo train and reconstruct a three-dimensional spatial estimate of the magnetization density $\hat{m}$ for that echo. This grouping process, which is diagrammed in Fig. 4a, is referred to as *time binning* since the samples of a given time interval in the echo train are grouped together for reconstruction. Note that there is a unique time bin ($b = 0$) which is a FID since it consists of data acquired during the sampling interval ranging from $t' = 0$ to the time the k trajectory reaches $k_{\max}$. Figure 4a also shows an alternative grouping b' which does not contain an explicit FID time bin.

The reconstruction method employs the Fourier-gridding algorithm (*22, 23*) for both its generality and ease of implementation. The sampled data which comprise bin b are designated by $r_b(p, n)$, where p is the projection index and n is the sample time index ($t' = n\Delta t$). Gridding involves first dividing $r_b(p, n)$ by the sampling density W, interpolating to a rectilinear grid using a convolution kernel $C(k)$, Fourier transforming to the spatial domain (using a fast algorithm), and then correcting for the effects of the convolution process in the spatial domain (undoming). Symbolically, the grid-

ding procedure which estimates the spatially dependent magnetization density $\hat{m}_b(\mathbf{r})$ for time bin b is written

$$\hat{m}_b(\mathbf{r}) = c^{-1}(\mathbf{r}) \cdot \sum_{\mathbf{k}_{\text{rect}}} \sum_{p,n} \frac{r_b(p,n)}{W(n)} C[\mathbf{k}_{\text{rect}} - \mathbf{k}(p,n)] e^{i2\pi \mathbf{k}_{\text{rect}} \cdot \mathbf{r}}, \quad [8]$$

where $\mathbf{k}_{\text{rect}}$ is the k-space rectilinear grid that is resampled to enable fast Fourier transformation to the spatial domain; $c^{-1}(\mathbf{r})$ is the reciprocal of the spatial Fourier transform of $C(\mathbf{k})$. The k-space sampling density $W(n)$ is spherically symmetric and hence is a function only of sample time n and not of the projection index p. Reconstruction aliasing artifacts which result from convolution and resampling in the k domain can be minimized in two ways (*23*): (1) by selecting an appropriate convolution kernel $C(k)$ and (2) by subsampling in the k domain so that the spacing of $\mathbf{k}_{\text{rect}}$ is smaller than 1/FOV. With suitable selection of these gridding parameters, point-spread function and SNR analyses may be performed using continuous-domain approximations.

The next three subsections describe reconstruction techniques and resulting point-spread functions for three cases: (1) reconstruction of the FID image ($b = 0$); (2) reconstruction of many time-binned echoes to create a spatially localized T_2^* map; and (3) full spatial/spectral reconstruction for chemical-shift imaging.

Point-Spread Function Analysis for a Time-Binned Echo as a Function of Chemical Shift and T_2^* Relaxation Time

The spatial point-spread function (PSF) resulting from the reconstruction of a single binned echo will be a function of $k_{\max}$, local off-resonance effects ω_l, the transverse relaxation time constant T_2^*, and any applied reconstruction filter $H(k_r)$.

Assuming linearity and shift invariance, the spatial PSF can be calculated by setting the source object m equal to the Dirac delta function [$m(x, y, z) = \delta(x, y, z)$], evaluating the received signal for a given k-space trajectory, and then determining the shape of the resulting reconstructed image (*24, 25*). In this manner, the effects of such processes as T_2^* relaxation and local off-resonance frequency shifts (ω_l) can be evaluated (*26–28*).

The proposed 3D oscillating gradient experiments possess a spherically symmetric k-space sampling density. From Eq. [6], the resulting T_2^*- and ω_l-dependent k-domain response function M, written as a function of t', to the test delta function m is

$$M(t'; k_x, k_y, k_z) = M(t'; k_r) = e^{-t'(k_r)/T_2^*} e^{i\omega_l t(k_r)}, \quad [9]$$

where $k_r = \sqrt{k_x^2 + k_y^2 + k_z^2}$. When no k-space filtering is applied, the reconstructed PSF is the spatial Fourier transform of Eq. [9].

The 3D Fourier transform of the spherically symmetric function $H(k_r)M(k_r)$ which is zero for $k_r > k_{\max}$ is (*29*)

$$\text{PSF}(r) = \frac{3}{k_{\max}^3} \int_0^{k_{\max}} H(k_r) M(k_r) \text{sinc}(2rk_r) k_r^2 dk_r, \quad [10]$$

where we have normalized for the volume of the k-space sphere. $H(k_r)$ is the applied k-space window function and $M(k_r)$ is given by Eq. [9].

For the case of an on-resonance spin ($\omega_l = 0$) with infinite T_2^* and no filtering [$H(k_r) = 1$], Eq. [10] yields PSF_{ball} which is the Fourier transform of a solid ball (*29*):

$$\text{PSF}_{\text{ball}}(r) = 3[\sin(2\pi r k_{\max}) - 2\pi r k_{\max} \cos(2\pi r k_{\max})]/(2\pi r k_{\max})^3. \quad [11]$$

Given a value for $k_{\max}$ (cm^{-1}), the full width at half-maximum (FWHM) of PSF_{ball} is approximately $0.8/k_{\max}$ (cm) and the nominal volume resolution is $\pi \text{FWHM}^3/6 = 0.27/k_{\max}^3$ (cm^3).

The next two subsections analyze the effects separately of T_2^* and ω_l upon the PSF for the RFa and RFb FID ($b = 0$) images. This is important both because we are interested in short-T_2 species and because these derived point-spread functions are the building blocks for constructing the full spatial–temporal and spatial–spectral point-spread functions.

T_2^*-dependent PSF for the FID image ($b = 0$). The effect of T_2^* upon the FID image ($b = 0$) is to act as a low-pass filter and hence broaden the PSF. The radial k-space position, written as a function of time, for the RFa excitation sequence is given by Eq. [3]. Assuming that sampling starts directly after application of the RF pulse, then the binned $b = 0$ RFa data are collected in time from $0 \leq t' \leq \pi/(2\Omega_0)$. From Eq. [9], the k-domain signal $M(k_r, T_2^*)$ for an on-resonance spin with transverse relaxation time constant T_2^* is

RFa:

$$M(k_r, T_2^*) = \exp\left[-\frac{1}{T_2^* \Omega_0} \sin^{-1}\left(\frac{k_r}{k_{\max}} \right) \right], \quad [12]$$

$$0 \leq k_r \leq k_{\max}$$

$$= 0, \quad k_r > k_{\max}.$$

The T_2^*-dependent RFa spatial PSF is calculated by substituting Eq. [12] into Eq. [10]. The result is derived in the Appendix and is denoted as $\text{PSF}_{\text{RFa}}(r, a)$ (Eq. [A4]) which is a convergent series of odd-order Bessel functions (J). The T_2^*-dependent parameter a is given by $a = 1/(2\pi\tau)$,

where τ relates T_2^* to the gradient-oscillation frequency f_0 (Hz),

$$\tau = T_2^* f_0, \qquad [13]$$

where $f_0 = \Omega_0/2\pi$.

The received T_2^*-dependent k-domain signal using RFb excitation for an on-resonance spin is

RFb:

$$M(k_r, T_2^*) = \exp\left[-\frac{1}{T_2^* \Omega_0} \cos^{-1}\left(1 - 2\frac{k_r}{k_{max}}\right)\right],$$

$$0 \leq k_r \leq k_{max}. \qquad [14]$$

The RFb spatial PSF for the $b = 0$ image, calculated by substituting Eq. [14] into Eq. [10], is a convergent series of even- and odd-order Bessel functions (Appendix, Eq. [A5]) and is denoted as $\mathrm{PSF}_{\mathrm{RFb}}(r, a)$. As with the RFa sequence, $a = 1/(2\pi\tau)$.

For no T_2 relaxation ($a = 0$), $\mathrm{PSF}_{\mathrm{RFa}}(r, 0) = \mathrm{PSF}_{\mathrm{RFb}}(r, 0) = \mathrm{PSF}_{\mathrm{ball}}(r)$. As T_2^* decreases, the relaxation process broadens the RFa and RFb point-spread functions albeit by slightly different amounts. This effect is shown in Fig. 5 with simulated data points overlaid upon the theoretical curves. For both sequences, three PSFs are plotted. The first curve is $\mathrm{PSF}_{\mathrm{ball}}$ (Eq. [11]). The second curve is for T_2^* equal to the time of the first gradient echo (RFa, $\tau = 1/2$; RFb, $\tau = 1$) and the third curve is for T_2^* equal to the time required to reach k_{max} from the origin (RFa, $\tau = 1/4$; RFb, $\tau = 1/2$). The simulation was performed with the following parameters: $N_{rf} = 1300$, $f_0 = 500$ Hz, and $k_{max} = 1$ cm^{-1}. Fourier-gridding reconstruction was implemented with a Kaiser–Bessel convolution kernel (*30*) ($\beta = 12$) and a factor of two subsampling. Figure 5 shows that the theoretical and simulated results are indistinguishable, suggesting that the continuous-domain PSF approximation is valid and that suitable parameters have been chosen for the gridding operation.

For equivalent relaxation, there is slightly more (5–10%) PSF volume broadening (decrease of nominal resolution) associated with RFb than with RFa. This difference results from RFb's higher sampling density at the k-space origin which causes the T_2 relaxation process to increase the relative attenuation of midrange and higher spatial frequencies.

Frequency-dependent PSF for the FID image ($b = 0$). From Eq. [9] and Eqs. [3] and [4], the k-domain signal $M(k_r, \omega_l)$ for an off-resonance spin with frequency shift ω_l is

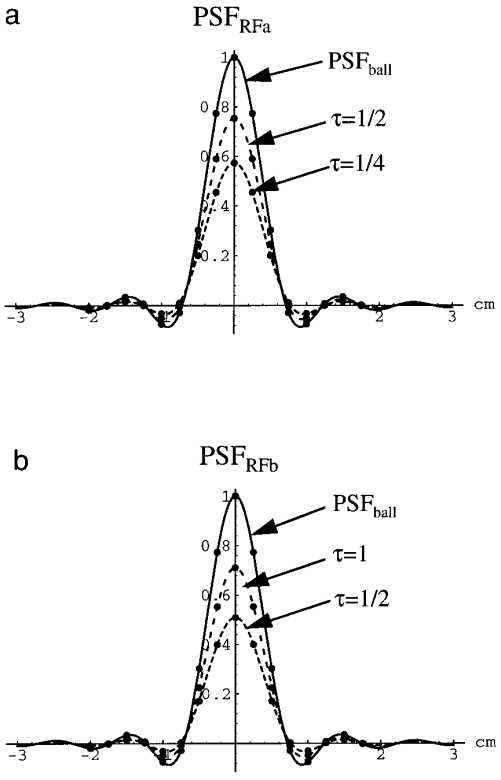

FIG. 5. The effect of T_2^* upon the $b = 0$ point-spread function for RFa excitation (a) and RFb excitation (b) with $k_{max} = 1$ cm^{-1}. Equivalent amounts of relaxation relative to the time k_{max} is reached are shown—(RFa, $\tau = 1/2$; RFb, $\tau = 1$), (RFa, $\tau = 1/4$; RFb, $\tau = 1/2$). The relative intensity of the PSF at the origin is indicative of the amount of PSF broadening as the asymptotic volume of the PSF is conserved independently of T_2^*. The RFb PSFs are 5–10% more broadened by transverse relaxation processes due to sampling-density differences. Simulated data are shown as dots superimposed upon the theoretical curves.

RFa:

$$M(k_r, \omega_l) = \exp\left[\frac{i\omega_l}{\Omega_0} \sin^{-1}\left(\frac{k_r}{k_{max}}\right)\right],$$

$$0 \leq k_r \leq k_{max}, \qquad [15]$$

RFb:

$$M(k_r, \omega_l) = \exp\left[\frac{i\omega_l}{\Omega_0} \cos^{-1}\left(1 - 2*\frac{k_r}{k_{max}}\right)\right],$$

$$0 \leq k_r \leq k_{max}. \qquad [16]$$

The off-resonance PSFs are obtained by substituting Eqs. [15] and [16] into Eq. [10]. Using the methods of the Appendix, the RFa PSF takes a form similar to the T_2^*-dependent PSF (Eq. [A4]) and is $\mathrm{PSF}_{\mathrm{RFa}}(r, a = -if)$, where $f = \omega_l/\Omega_0$ relates the amount of frequency shift to the gradi-

ent-oscillation frequency. The frequency-dependent RFb PSF is $PSF_{RFb}(r, a = -if)$ by Eq. [A5].

The off-resonance PSFs are complex, with the imaginary part, which tends to be high pass, increasing as f also increases. Analogously to the T_2^* results, it can be shown that, compared with RFa, the RFb PSF is 10–15% more corrupted by equivalent amounts of frequency shift. However, for $f < 0.1$, PSF corruption can be considered negligible (<5%) in both cases. For larger values of f, it is still possible to reduce point-spread function distortion when reconstructing with one chemical-shift species per voxel by either (1) iteratively minimizing the imaginary component of a reconstructed localized region via demodulation of the received signal (*27*), or (2) demodulating the k-domain signal based upon *a priori* knowledge of the spatial distribution of the B_0 field.

Incorporation of Multiple Echoes to Measure T_2^*

An important application of the proposed imaging schemes is the reconstruction of multiple gradient echoes to spatially localize T_2^*. As shown in Fig. 4a, for each of the N_b full-echo groupings $b = 1, 2, \ldots, N_b$ ($b \neq 0$), each point in k space is sampled twice. This occurs since the k trajectory both emanates from and returns to the k-space origin within a single full-echo time-bin interval. As the dual sampling is symmetric in time about the echo center, the effects of the T_2^* decay process upon the PSF tend to be mitigated.

For RFa, the gradient echoes occur at times $t'_b = b\pi/\Omega_0$. The dual sampling causes the binned k-space signal to have two terms both weighted by $\exp(-t'_b/T_2^*)$,

RFa:

$$M(k_r, b) = \exp\left(-\frac{t'_b}{T_2^*}\right) \times \left[\left(\exp\left[-\frac{1}{T_2^*\Omega_0}\sin^{-1}\left(\frac{k_r}{k_{max}}\right)\right]\right) + \left(\exp\left[+\frac{1}{T_2^*\Omega_0}\sin^{-1}\left(\frac{k_r}{k_{max}}\right)\right]\right)\right], \quad [17]$$

for $b = 1, 2, \ldots, N_b$, and $0 \leq k_r \leq k_{max}$. Off-resonance effects are neglected.

The first term of Eq. [17] possesses a similar type of low-pass T_2^* dependence as shown in Eq. [12] for the $b = 0$ time bin. In contrast, the sign of the exponential of the second term is positive, indicating relatively enhanced high-spatial-frequency components. After spatial Fourier transform of Eq. [17], the resulting RFa PSF for a full-echo image, by Eq. [A4], is

$$PSF_{RFa}(r, b, a) = e^{-b/2\tau}[PSF_{RFa}(r, a) + PSF_{RFa}(r, -a)], \quad [18]$$

where $\tau = T_2^* f_0$ as defined in Eq. [13] and $a = 1/(2\pi\tau)$. For RFb, the echoes occur at times $t'_b = b2\pi/\Omega_0$ and the PSF by Eq. [A5] is

$$PSF_{RFb}(r, b, a) = e^{-b/\tau}[PSF_{RFb}(r, a) + PSF_{RFb}(r, -a)]. \quad [19]$$

Equations [18] and [19] demonstrate that a sequence of images following a decay curve given by $e^{-b/(2\tau)}$ (for RFa) and $e^{-b/\tau}$ (for RFb) is created. For each image, the series of Bessel functions which comprise the spatial point-spread functions are summed with both positive and negative values of the T_2^*-dependent parameter—a. This causes first-order cancellation of the PSF shape dependence upon the transverse relaxation rate. Even for short values of T_2^*, the degradation of the full-echo PSFs is small. For example, for T_2^* equal to the time of the first echo (RFa, $\tau = 1/2$; RFb, $\tau = 1$), the full-echo point-spread functions are within 5% of PSF_{ball} whereas the FID ($b = 0$) PSF is volume broadened by over 30% (Fig. 5).

A spatial T_2^* estimate for a full k-space scan may be generated by creating a complete sequence of images ($b = 0, 1, 2, \ldots, N_b$) with the $b = 0$ image multiplied by two to normalize for the double sampling of the full-echo images. Each voxel will then have associated with it a FID which can be fit to a decay curve. However, in attempting to quantify the transverse decay time constants and signal intensities, it may become important to consider the effects of the different T_2^*-dependent PSFs for the FID ($b = 0$) and full-echo images ($b = 1, 2, \ldots, N_b$).

Figure 4a also shows an alternative grouping b' which does not consist of an explicit FID image. Using this grouping, relatively enhanced high- and low-spatial-frequency signals are also combined with the high-pass signal weighted less as determined by τ. The point-spread functions are

$$PSF_{RFa}(r, b', a) = e^{-b'/2\tau}[PSF_{RFa}(r, a) + e^{-1/2\tau} \cdot PSF_{RFa}(r, -a)] \quad [20]$$

$$PSF_{RFb}(r, b', a) = e^{-b'/\tau}[PSF_{RFb}(r, a) + e^{-1/\tau} \cdot PSF_{RFb}(r, -a)], \quad [21]$$

where $a = 1/(2\pi\tau)$, $b' = 0, 1, 2, \ldots, N_b - 1$.

The b' grouping also causes the shape of the PSF to be relatively T_2^*-independent while moving the effective time position of image b' to time $t'_{b'} = (t'_b + t'_{b+1})/2$. Thus, the time of the first bin in the b' temporal time sequence ($b' = 0$) coincides with the time k_{max} is reached.

The choice of which combination of the b and b' groupings to use for spatial–temporal reconstruction may depend upon several factors, including the shortest value of τ, the signal power-spectral-density function, and the SNR. Figure 6 shows

b and b' grouped points (for RFb) created for a voxel centered in a uniform sphere with diameter of $1/(2k_{max})$ and a transverse relaxation value of $\tau = 1$. Superimposed is the theoretical monoexponential decay curve. The intensity of the $b = 0$ point is reduced by 30% from the theoretical value. This error can skew both intensity and T_2^* estimates. In comparison, the full-echo b and b' points are within 5% of the theoretical value. Although the above results may suggest excluding the $b = 0$ image or using just the b' groupings to estimate the signal intensity, this may not yield superior results as the goal is to estimate the signal intensity at $t = 0$. These issues are further discussed in later sections.

Spatial–Spectral Reconstruction

A complete spatial–spectral (4D) image estimate can be generated using the Fourier-gridding algorithm coupled with the k-FID approach (*31*) to spectral estimation. Here, each sampled point in k space is regarded as having a FID associated with it as is shown in Fig. 4b. To reconstruct, each k-FID is Fourier transformed in the time domain (k_ω space) to produce a k spectrum. A linear phase correction is then applied to each k spectrum to unwrap the phase accumulated before the starting sampling time $t_0'(k)$ of the k-FID. The phase-corrected k spectra are then spatially Fourier transformed, using gridding, to produce a spatial/spectral estimate.

From Eq. [8], the k-FID/gridding image estimate is written as

$$\hat{m}_{k\mathrm{FID}}(\mathbf{r}, \omega) = c^{-1}(\mathbf{r}) \sum_{\mathbf{k}_{\mathrm{rect}}} e^{i2\pi \mathbf{k}_{\mathrm{rect}} \cdot \mathbf{r}} \left[e^{-it_0'(\mathbf{k}_{\mathrm{rect}}) \cdot \omega} \sum_{b'=0}^{N_b} \left\{ \sum_{p,n} \frac{r_b(p, n)}{W(n)} C[\mathbf{k}_{\mathrm{rect}} - \mathbf{k}(p, n)] \right\} e^{-i\omega b' \Delta t_{k\mathrm{FID}}} \right], \quad [22]$$

where $\Delta t_{k\mathrm{FID}}$ is the time separation of the k-FID samples.

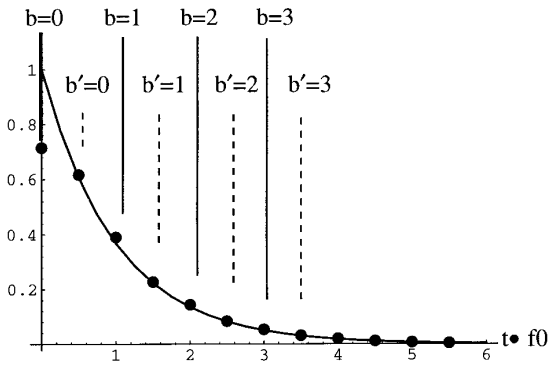

FIG. 6. A decay curve showing b and b' sample points (for RFb) created for a voxel centered in a uniform sphere with diameter equal to $1/(2k_{max})$ and transverse relaxation value of $\tau = 1$. Superimposed is the theoretical monoexponential decay curve. The intensity of the $b = 0$ sample point is reduced by 30%.

For a full k-space scan, $\Delta t_{k\mathrm{FID}} = \pi/\Omega_0$ (for RFa) and $\Delta t_{k\mathrm{FID}} = 2\pi/\Omega_0$ (for RFb). For the continuously oscillating/rotating experiment (GR_{ss}), the k data should be gridded before the Fourier transforms of the k-FIDs are performed (Eq. [22]). For GR_{sp}, the k-FIDs of each discrete projection may be processed before gridding.

The spatial/spectral point-spread function can be determined by analyzing the response to a 4D impulse function $\delta(x, y, z, \omega - \omega_1)$ while also considering T_2^* relaxation. The first reconstruction step is the discrete-time Fourier transform of the sampled k-FIDs including the phase correction applied in the spectral domain given by $e^{-it_0'(k_r)\cdot\omega}$,

$$\begin{aligned} M(t_0'\colon k_r, \omega, T_2^*) &= e^{-t_0'(k_r)\cdot(i\Delta\omega + 1/T_2^*)} \\ &\quad \times \sum_{b'=0}^{N_b} e^{-(b'\Delta t_{k\mathrm{FID}})\cdot(i\Delta\omega + 1/T_2^*)} \\ &\approx \frac{e^{-t_0'(k_r)\cdot(i\Delta\omega + 1/T_2^*)}}{1 - e^{-(\Delta t_{k\mathrm{FID}})(i\Delta\omega + 1/T_2^*)}}, \end{aligned} \quad [23]$$

where $\Delta\omega = \omega - \omega_1$, and we assume that the total sampling time is longer than T_2^*.

The b' indexing is used since there are two k-FIDs for each radial point in k-space—one that starts when the trajectory is emanating from the origin to k_{max} and the other when it returns (Fig. 4b). These two starting times $t_{01}'(k_r)$ and $t_{02}'(k_r)$ for the RFb scan sequence are

$$\begin{aligned} t_{01}'(k_r) &= \frac{1}{\Omega_0} \cos^{-1}\left(1 - 2\frac{k_r}{k_{max}}\right), \\ t_{02}'(k_r) &= \frac{2\pi}{\Omega_0} - \frac{1}{\Omega_0} \cos^{-1}\left(1 - 2\frac{k_r}{k_{max}}\right). \end{aligned} \quad [24]$$

Substituting $t_{01}'(k_r)$ and $t_{02}'(k_r)$ into Eq. [23] and summing the result, the RFb response is

$$\begin{aligned} &M_{\mathrm{RFb}}(k_r, \Delta f, \tau) \\ &= \frac{\exp\left[-(i\Delta f + 1/\tau)\cos^{-1}\left(1 - 2\frac{k_r}{k_{max}}\right)\right]}{1 - e^{-(i2\pi\Delta f + 1/\tau)}} \\ &\quad + \frac{\exp\left[(i\Delta f + 1/\tau)\cos^{-1}\left(1 - 2\frac{k_r}{k_{max}}\right)\right]}{[e^{(i2\pi\Delta f + 1/\tau)}][1 - e^{-(i2\pi\Delta f + 1/\tau)}]}, \end{aligned} \quad [25]$$

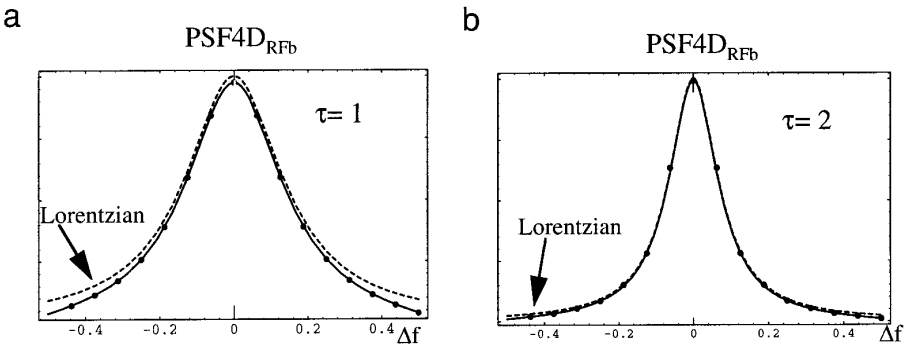

FIG. 7. Absorption lineshapes for the RFb sequence given by Eq. [26] for two values of τ. Simulated data are shown as dots superimposed upon the theoretical curves. The Lorentzians show lineshape distortion caused when τ is small.

where $\tau = T_2^* f_0$ as previously defined. For the 4D reconstruction, $\Delta f = \Delta\omega/\Omega_0$ is the independent coordinate used to measure the spectral lineshape. Note that the numerators of Eq. [25] have a form similar to Eqs. [14] and [16] which describe the T_2^* and off-resonance dependences of the $b = 0$ k-domain signal. Thus, after the spatial Fourier transform of Eq. [25], the resulting 4D PSF is

$$\mathrm{PSF4D_{RFb}}(r, \Delta f, \tau) = \frac{1}{1 - e^{-(i2\pi\Delta f + 1/\tau)}} [\mathrm{PSF_{RFb}}(r, a) + e^{-(i2\pi\Delta f + 1/\tau)}\mathrm{PSF_{RFb}}(r, -a)], \quad [26]$$

where $a = 1/(2\pi\tau) + i\Delta f$ is dependent upon both T_2^* and Δf and $\mathrm{PSF_{RFb}}$ is given by Eq. [A5]. The realizable spectral bandwidth is $2\pi/\Omega_0$.

Equation [26] shows that, within the allowable spectral bandwidth, the spectral–spatial PSF is invariant to absolute chemical shift ω_1. The spatial PSF is relatively independent of T_2^*, similar to the b' grouped images discussed previously (Eq. [21]). In the spectral domain there is some lineshape distortion for short T_2^* moieties resulting from the unique starting sampling time of each k-space point and the upper bound on the realizable spectral bandwidth. This distortion is demonstrated in Fig. 7a which shows theoretical and simulated absorption lineshapes as well as the ideal Lorentzian curve for $\tau = 1$. Figure 7b demonstrates that for τ as small as 2, the Lorentzian and oscillating gradient lineshapes are virtually identical.

The RFa 4D PSF is

$$\mathrm{PSF4D_{RFa}}(r, \Delta f, \tau) = \frac{1}{1 - e^{-(i\pi\Delta f + 1/2\tau)}} [\mathrm{PSF_{RFa}}(r, a) + e^{-(i\pi\Delta f + 1/2\tau)}\mathrm{PSF_{RFa}}(r, -a)]. \quad [27]$$

For a full k-space scan, the RFa realizable spectral bandwidth is $4\pi/\Omega_0$, which is twice that provided by the RFb sequence. Yet, for equivalent spatial resolution, twice as much gradient magnitude and slew rate capability is required.

Signal and Noise Analysis

The theoretical noise power-spectral-density function (PSD) and signal-to-noise ratio of an MRI experiment may be calculated, given knowledge of the properties of the received noise, the imaging time T_{exp}, the sampling density W, and the reconstruction filter H.

The ensuing analysis assumes that the received signal $r(t)$ is composed of the true NMR signal $s(t)$ plus uncorrelated noise $q(t)$ with variance σ_t^2 so that $E[q(t_1)q(t_2)] = \sigma_t^2\delta(t_1 - t_2)$ (*32*). Assuming no gridding artifacts, the reconstructed noise power-spectral-density function $\mathrm{PSD}(k_r) = \sigma_t^2 H(k_r)^2/W(k_r)$ (*33*). From Parseval's theorem, the reconstruction noise variance in the spatial domain σ_r^2 is the volume integral of the noise PSD over k space:

$$\sigma_r^2 = \sigma_t^2 \int_k \frac{H(k_r)^2}{W(k_r)}\, dk. \quad [28]$$

As part of the SNR analysis, we will examine the effects of a Gaussian low-pass window which may be incorporated into the reconstruction process,

$$H(k_r) = \exp[-g(k_r^2/k_{max}^2)], \quad [29]$$

where g determines the amount of filtering applied ($g = 2.5$ approximates a Hanning window). The filter may be applied to reduce truncation artifacts, reduce the differential effects of multiple transverse relaxation rates upon the PSF, or improve SNR. The introduction of H here is just to show the relative effect of low-pass filtering upon the reconstruction noise magnitudes for the proposed excitation sequences. The specific influence of H upon the different T_2^*-dependent PSFs will not be addressed.

The sampling-density function $W(k_r)$ is defined as the sampling time per unit volume of k space and is normalized

so that its integral over the k-space volume is the total sampling time of the experiment T_{exp}. $W(k_r)$ can be calculated from two components: (1) the geometry of the k-space trajectory (e.g., projection reconstruction, CSI) and (2) the magnitude of the velocity of the sampling path which is proportional to the magnitude of the applied B_0 gradient field (*34*).

We will examine the variance of the reconstruction noise for both the RFa and RFb scenarios. For purposes of comparison, schemes which offer uniform sampling density (UNIF) such as phase-encoded CSI (*35*) will also be analyzed. The calculated sampling densities of the three experiments (RFa, RFb, UNIF) which sample a solid sphere in k space of radius k_{max} are

$$W_{RFa}(k_r) = T_{exp}/(2\pi^2 k_r^2 k_{max}\sqrt{1 - k_r^2/k_{max}^2}),$$
$$W_{RFb}(k_r) = T_{exp}/[2\pi^2 k_r^2 k_{max}\sqrt{1 - (1 - 2k_r/k_{max})^2}],$$
$$W_{unif}(k_r) = 3T_{exp}/(4\pi k_{max}^3).$$

Figure 8a shows the three resulting noise PSDs with no window function applied [$H(k_r) = 1$]. Due to the projection geometry, the relative noise PSD is elevated at midrange and higher spatial frequencies for both the RFa and RFb excitation sequences. Such differences will affect relative sensitivity to edges and the overall SNR (*36*). Figure 8b shows a plot of the ratios of the RFa and RFb theoretical noise variances (σ_r^2) to that yielded by uniform sampling. These ratios are plotted as a function of g and were generated by numerically integrating Eq. [28]. For no filtering ($g = 0$), the RFa reconstruction noise variance is 40% higher than that yielded by uniform sampling and the RFb variance is 80% higher. As g increases, causing the amount of low-pass filtering to also increase, the sampling densities offered by the 3D projection experiments approach the ideal matched Gaussian density and the relative SNRs improve. In comparing RFa with RFb, note that the RFa image noise variance is always lower due to its sampling-density superiority.

Figure 8b shows that, when not accounting for T_2^* decay, the 3D oscillating gradient experiment may offer inferior SNR to that provided by uniform sampling especially when little or no k-space filtering is performed. However, even in these cases, significant SNR gains can be achieved for short-T_2 species. The conditions for when the 3D oscillating gradient experiments are advantageous can be calculated by accounting for the signal loss given by $\exp(-t_{phs}/T_2^*)$ when a phase-encode gradient of duration t_{phs} is required as for CSI. With no filtering ($g = 0$), the uniform sampling and oscillating gradients offer equivalent SNRs when $t_{phs} = 0.17T_2^*$ (for RFa) and $t_{phs} = 0.29T_2^*$ (for RFb). For instances when $t_{phs} > T_2^*$, there will be more than a factor of two SNR gain provided by both RFa and RFb. It must also be reiterated that the CSI experiment may not even be tenable for a large FOV given imaging-time constraints. Oscillating gradient techniques which scan k space rectilinearly (*19*) also require a phase-encode gradient.

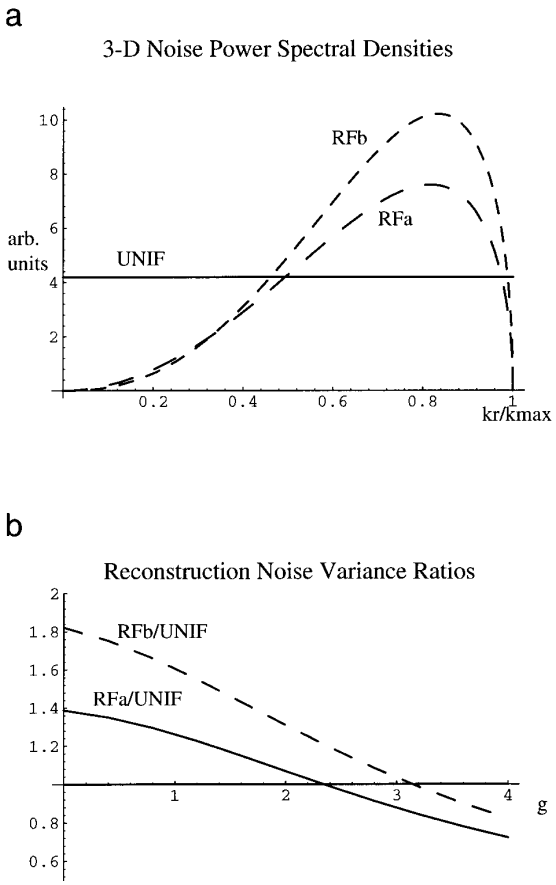

FIG. 8. (a) 3D noise power spectral densities (PSD) corresponding to uniform sampling (UNIF), and the RFa and RFb sequences. The increased noise PSD for RFa and RFb at midrange and higher spatial frequencies is a function of gradient waveform shape and projection geometry. (b) Ratios of the reconstruction noise variances (σ_r^2) comparing RFa and RFb sequences with uniform sampling density. The ratios are plotted as a function of g, the Gaussian filtering parameter $\{H(k_r) = \exp[-g(k_r^2/k_{max}^2)]\}$.

RF Excitation and Steady-State Magnetization

The two gradient trajectories GR_{ss} and GR_{sp} offer different contrast mechanisms with different sensitivities. The continuously oscillating/rotating trajectory GR_{ss} is a steady-state free-precession (SSFP) sequence yielding a complicated contrast dependence upon flip angle, T_1, T_2, chemical shift, and B_0 inhomogeneities (*37*, *38*). Of particular importance is the phase advance θ_0 of an isochromat between successive RF pulses. θ_0 is composed of two additive parts ($\theta_0 = \theta_{0b} + \theta_{0r}$): (1) θ_{0b}, caused by chemical shift and B_0 inhomogeneities; and (2) θ_{0r}, caused by applied RF phase changes.

The most popular classes of SSFP imaging techniques are known as refocusing sequences and scan a rectilinear k-

space trajectory in a manner where only the phase-encode gradient is rewound (*39–42*). Since the readout gradient is not rewound, θ_{0b} ranges uniformly between 0 and 2π within a given voxel and the signal magnitude is neither chemical-shift- nor B_0-dependent. In general, the contrast dependence goes as T_2/T_1.

If T_R is sufficiently short and the magnet is sufficiently well shimmed, the so-called uniform-field condition may be met where θ_{0b} is small. It is then possible to consider SSFP imaging using GR_{ss}, where all the gradients are rewound and the trajectory returns to $k = 0$ at the application of each successive RF pulse. Sekihara (*43*) has shown theoretically that, under the uniform-field condition, the sensitivity of the SSFP experiment may be significantly greater than that for the refocusing or spoiled sequences. In this case, maximum contrast immunity to residual B_0 inhomogeneities θ_{0b} occurs if the phase of the RF pulse is advanced 180° ($\theta_{0r} = \pi$) from pulse to pulse, which is known as alternating-pulse steady-state free precession (AP-SSFP). Still, T_R must be less than the time it takes for the spins to dephase ±90° ($|\theta_{0b}| < \pi/2$).

When $\theta_{0r} = \pi$, the optimum flip angle α_{op} and maximum signal magnitude M_{max} are (*37*)

$$\alpha_{op} = \cos^{-1}\left(\frac{E_1 - E_2}{1 - E_1E_2}\right),$$

$$M_{max} = M_0\sqrt{\frac{1 - E_1}{(1 + E_1)(1 - E_2^2)}}, \qquad [30]$$

where $E_1 = \exp(-T_R/T_1)$, $E_2 = \exp(-T_R/T_2)$, and M_0 is the equilibrium magnetization value.

To image a system with multiple spectral lines, T_R can be set such that all moieties align themselves in phase just before the application of each RF pulse (*43*). With GR_{ss}, this means setting the frequency of the oscillating gradient appropriately. GR_{ss} AP-SSFP spectroscopic imaging is most practical when a minimal number of spectral lines are present (e.g., fat and water) and where high spectral resolution is not desired. For example, at 2.35 T (100 MHz) and allowing for a B_0 inhomogeneity of 0.5 ppm, a maximum T_R of 10 ms is permitted. If the separation of fat and water is approximately 3.6 ppm, then T_R may be 2.78, 5.56, or 8.33 ms.

GR_{sp} may be run in either a refocused or a spoiled mode depending upon the crusher gradient implementation and whether RF spoiling techniques (*44*) are incorporated. As a spoiled sequence, contrast will dependent solely upon T_1, T_R, and flip angle. The maximum signal, M_E, is attained with the flip angle equal to the Ernst angle α_E:

$$\alpha_E = \cos^{-1}(E_1), \quad M_E = M_0\sqrt{(1 - E_1)/(1 + E_1)}. \qquad [31]$$

If RF spoiling techniques are not utilized, contrast will tend to behave as for a refocused sequence where the phase-encode gradient is not rewound (*45*).

The maximum sensitivity of GR_{ss} (Eq. [30]) may be more that a factor of two higher than that offered by GR_{sp} (Eq. [31]) depending upon the relaxation and imaging parameters. However, the SSFP B_0 homogeneity restraints are very strict and may be easily violated by B_0 eddy currents, motion, and flow effects. Moreover, the short T_R requirements of the SSFP sequence may mean that the chemical-shift resolution will be too coarse.

EXPERIMENTAL METHODS

Several ^{1}H and ^{23}Na experiments were performed on a modified medium-bore Bruker 2.35 T spectrometer to demonstrate the feasibility of the continuously oscillating gradient techniques. The B_0 gradients were self-shielded with a maximum magnitude of 6 G/cm and maximum slew rate of over 20 G/cm/ms (*46*). The ^{1}H and ^{23}Na images were acquired using a 14 cm diameter dual-tuned birdcage coil based on a four-ring design (*47*). The maximum applied RF power was 1 kW. For the RFb excitation sequences, an RF pulse ranging in duration from 20 to 100 μs was applied, either just before or at the gradient zero. In all cases, the RFb pulse placement and/or finite duration caused the $k = 0$ time to be moved symmetrically slightly before and after the gradient zero. This shift was accounted for in the reconstruction process. The RFa pulse was centered exactly at the gradient maximum which, due to waveform symmetry, is the $k = 0$ time. Short probe ringdown times (<40 μs) were achieved in part by using an active Q-spoiling circuit (*48*). Reconstruction was performed on a Sun Sparc10 workstation (Sun Microsystems, Mountain View, California).

An important aspect of calibrating the system was to measure the phase lag between the programmed gradient waveform and the actual field. This information was then used to adjust the phase of the programmed waveform during scanning. The phase-calibration procedure used the GR_{sp} RFa sequence to sample the signal from a 1 cm diameter water sphere and is diagrammed in Fig. 9. The test phantom was placed in the isocenter of the magnet and shimmed. A sinusoidal gradient waveform was turned on and allowed to reach steady state and a hard RF pulse was applied at the gradient maximum. The positions of the peaks of the odd and even echoes were then measured. When the RF pulse is centered exactly at a gradient maximum then the odd and even echoes are equally spaced in time. By measuring the echo spacing, the programmed phase of the waveform was iteratively adjusted until the odd and even echoes were symmetric in time. The calibration was performed on the x, y, and z axes for all oscillation frequencies that were utilized experimentally. The odd and even peaks were adjusted to be equally spaced to within one-eighth of a readout sample with dwell time Δt as given by Eq. [5].

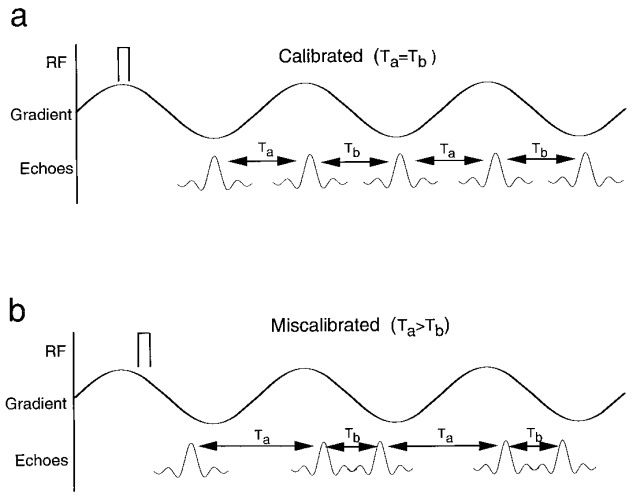

FIG. 9. The gradient-phase-calibration procedure. (a) The gradient phase is adjusted so that, when a hard RF pulse is applied, the spacings of the even and odd echoes are equivalent in time ($T_a = T_b$). (b) A gradient-phase error of approximately 20° and its resulting signal.

The experiments which are presented are: (1) water/lipid phantom scanned with the AP-SSFP GR_{ss} RFb sequence and with the GR_{sp} RFa sequence, (2) GR_{sp} RFb ^{23}Na acquisition of an *in vitro* rabbit heart and two reference vials, and (3) *in vivo* ^{1}H and ^{23}Na GR_{sp} RFb imaging of a human hand. For GR_{sp}, RF spoiling techniques were not implemented.

Water/Lipid Phantom Scanned with the AP-SSFP GR_{ss} RFb Sequence and with the GR_{sp} RFa Sequence

A ^{1}H phantom composed of two chemical-shift species was constructed and is shown in Fig. 10. The outer flood field contained a 4% by weight agarose gel which yielded a water resonance. The tubes (5 mm diameter) contained vegetable oil which yielded a lipid signal. The flood field was used to show variation of image intensity across the field of view while the lipid-filled tubes demonstrated spatial resolution.

The phantom was scanned first using the AP-SSFP GR_{ss} RFb sequence. The experiment was designed so that the CH_2 and water moieties dephase and then realign just before successive RF pulses. To achieve this rephasing, a gradient-oscillation frequency of $f_0 = 640$ Hz was chosen with four cycles elapsing between successive RF pulses. Since T_R was 6.25 ms, the maximum allowable B_0 inhomogeneity which still ensured uniform excitation with AP-SSFP excitation was ± 0.4 ppm.

The GR_{ss} RFb imaging parameters were $f_0 = 640$ Hz, $G_0 = 0.75$ G/cm, $k_{max} = 2.1$ cm^{-1}, $N_{rf} = 2000$, $T_R = 6.25$ ms, flip angle = 20°, and FOV = 12.8 cm. The gradient waveforms were calculated so that the *k*-space origin was traversed both 15 μs before and after the gradient zero. This allowed for the application of a 20 μs RF pulse (excitation bandwidth = 50 kHz) and probe ringdown to occur before $k = 0$ was sampled. The scanning time for a single full *k*-space sweep was 12.5 s. The total imaging time was 25 s since $N_{avg} = 2$, where N_{avg} is the number of scans averaged. Because of the short T_R, chemical-shift resolution was not very fine (0.83 ppm), allowing only for the differentiation between water and total lipid signals. The reconstructed FOV ($x \times y \times z$) was $12.8 \times 12.8 \times 6.4$ cm^3 on a $64 \times 64 \times 8$ matrix. A Gaussian filtering parameter ($g = 1$) was used which resulted in a spherically symmetric spatial PSF with a FWHM of 4 mm (0.03 cm^3 nominal resolution). A 53 Hz line-broadening filter was applied before the *k*-FID/gridding reconstruction.

The phantom was also scanned with GR_{sp} using excitation at a gradient maximum while sweeping the elevation angle from 0 to $\pi/2$ and still obtaining complete *k*-space coverage (RFa′). Spatial resolution for this experiment was more coarse than that with the GR_{ss} RFb experiment but spectral resolution was higher. The imaging parameters were $f_0 = 710$ Hz, $G_0 = 1.07$ G/cm, $k_{max} = 1.0$ cm^{-1}, $N_{rf} = 350$, $T_R = 200$ ms, flip angle = 10°, and FOV = 12.8 cm. The total imaging time was 140 s ($N_{avg} = 2$) for the full scan. The reconstructed FOV was $10 \times 10 \times 6.4$ cm^3 on a $64 \times 64 \times 8$ matrix and a Gaussian filtering parameter ($g = 1$) was used, resulting in a spatial PSF with a FWHM of 8 mm. The reconstructed bandwidth was 7.1 ppm and the spectral resolution was 0.14 ppm as the FID was sampled for 45 ms. Due to the RF pulse length (22 μs) and probe ringdown (40 μs), three points near the origin of *k* space could not be sampled. Hence, no samples comprising the $b = 0$ image ($t' = 0$ to $1/(4f_0)$—the first 350 μs) were used in the *k*-FID/gridding spatial/spectral reconstruction.

GR_{sp} RFb ^{23}Na Acquisition of an in Vitro Rabbit Heart with Two Reference Vials

The goal of the study was to determine how well the complex ^{23}Na transverse relaxation process could be characterized using continuously oscillating gradients to generate a spatial/temporal estimate.

A rabbit heart was placed in a test tube along with an isotonic NaCl solution as perfusate. To provide a monoexponential reference, two 1.7 cm diameter vials filled with 100 m*M* NaCl solutions with different T_2 values were imaged at the same time. The solvent in each tube was a volume/volume (v/v) mixture of glycerol and water. As the sodium spectrum was in the extreme-narrowing limit, the T_2 relaxation process was monoexponential and $T_1 \approx T_2$. The T_2 values of the two vials, measured independently using a nonlocalized spin-echo experiment, were 640 μs (86% glycerol v/v) and 4.4 ms (61% glycerol v/v), respectively.

The rabbit heart and two reference vials were scanned with the GR_{sp} RFb excitation sequence approximately one hour after cardiac arrest. The imaging parameters were $f_0 =$

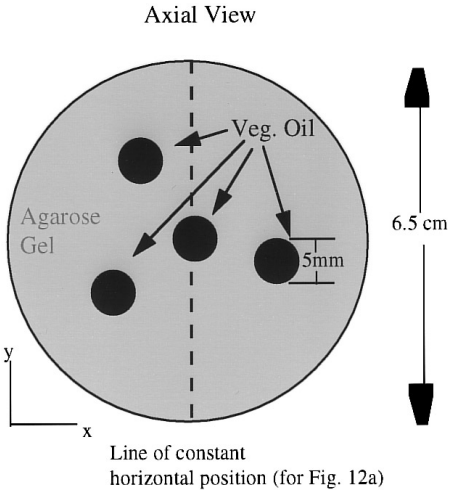

FIG. 10. Axial view of the ^{1}H test phantom composed of a 4% by weight agarose gel bath and four vegetable oil tubes.

800 Hz, $G_0 = 1.6$ G/cm, $k_{max} = 0.70$ cm^{-1}, $T_R = 50$ ms, flip angle = 70°, $N_{rf} = 1000$, and FOV = 10 cm. The imaging time per *k*-space sweep was 50 s and the total imaging time was 13 min ($N_{avg} = 16$). The RF pulse, centered at the gradient zero, was 100 μs in duration (excitation bandwidth = 10 kHz). Due to this finite bandwidth and accompanying small gradient magnitude, the $k = 0$ time occurred 30 μs before and after the gradient zero. Although the $k = 0$ point was not sampled for the $b = 0$ image, sampling was sufficiently dense near the *k*-space origin so as not to impact upon the PSF. No spatial filtering was used in reconstruction ($g = 0$) and the resulting PSF FWHM was 11 mm (0.70 cm^3). The sample was shimmed to within ±20 Hz ($f = 20/800 = 0.025$). Thus, there was little effect of B_0 inhomogeneities upon the spatial point-spread function [$PSF_{RFb}(r, a = -if)$]. A total of 16 echoes were saved ($N_b = 16$).

In Vivo ^{1}H and ^{23}Na GR_{sp} RFb Imaging of a Human Hand

An *in vivo* ^{1}H chemical-shift-resolved image was taken of the hand of a normal volunteer using GR_{sp} with excitation applied slightly before the gradient zero (RFb). The imaging parameters were $f_0 = 600$ Hz, $G_0 = 0.85$ G/cm, $k_{max} = 1.9$ cm^{-1}, $N_{rf} = 2400$, $T_R = 30$ ms, flip angle = 30°, and FOV = 14 cm. Total imaging time was 144 s ($N_{avg} = 2$). The RF pulse duration was 20 μs and was centered 11 μs before the gradient zero. The PSF FWHM was 4 mm (0.03 cm^3) and the spectral resolution was 0.27 ppm with an observable bandwidth of 6 ppm.

After acquisition of the ^{1}H images, ^{23}Na images of the hand were acquired using the GR_{sp} RFb excitation sequence. The total imaging time was 27 min ($N_{avg} = 32$) and the imaging parameters were $f_0 = 500$ Hz, $G_0 = 1.0$ G/cm, $k_{max} = 0.7$ cm^{-1}, $N_{rf} = 1000$, $T_R = 50$ ms, flip angle = 70°, and FOV = 14 cm. The RF pulse of duration 100 μs was centered at the gradient zero. No spatial filtering was used and the FWHM of the spatial PSF was 11 mm (0.70 cm^3). Eight echoes were saved ($N_b = 8$).

EXPERIMENTAL RESULTS

Water/Lipid Phantom Scanned with the AP-SSFP GR_{ss} RFb Sequence and with the GR_{sp} RFa Sequence

Figure 11 shows a spatial/spectral reconstruction of the water/lipid phantom from the 4D data set taken with the GR_{ss} sequence. Each image represents a spectral bin with a width of 83 Hz of a central 8 mm axial slice. Although the spectral resolution is coarse, the lipid and water resonances are well separated. The image intensity is uniform to within 10%, indicating that the B_0-uniform-field condition was not violated. Spatial resolution is consistent with the predicted value (0.03 cm^3).

The data taken with the GR_{sp} RFa′ sequence are also presented. Figure 12a shows a spatial/spectral surface plot of intensity vs chemical shift and position along the vertical line shown in Fig. 10 for a central slice in *z*. The surface plot demonstrates both the spatial and the spectral resolution. It is seen that for the imaging parameters used, the water signal bleeds into the region where the vegetable oil tube is located. Figure 12b shows an absorption spectrum from a voxel containing lipid and water signals. The spectral resolution is sufficient so that CH, CH_2, and CH_3 proton signals are all visible. Broad CH_2 lines from protons located near double bonds of the unsaturated vegetable oil are also evidenced. The slight baseline offset results from the missing points not sampled at the beginning of the FID along with the sampling properties of the RFa′ trajectory.

GR_{sp} RFb ^{23}Na Acquisition of an in Vitro Rabbit Heart with Two Reference Vials

Figure 13a shows a reconstructed, time-binned, ^{23}Na axial slice demonstrating the position of the two vials as well as the rabbit heart. Figure 13b shows reconstructed FIDs from voxels positioned at the center of each of the three regions of interest. Both the *b* and *b*′ groupings were used to generate the FID points with the display being similar to that shown in Fig. 6. The ordinate scaling is normalized so that a 100 m*M* ^{23}Na concentration corresponds to a value of 1. The FIDs from vials 1 and 2 were fitted to monoexponential curves while the FID from the rabbit heart was fitted to a biexponential curve using a Levenberg–Marquardt nonlinear fitting routine (*49*). For each voxel, three fits were performed to evaluate the *b* and *b*′ groupings separately as well as the two groupings together. The results are shown in Table 1. Overall, the *b* grouping alone and the *b* and *b*′ groupings combined yielded the best estimates. The results are further analyzed under Discussion.

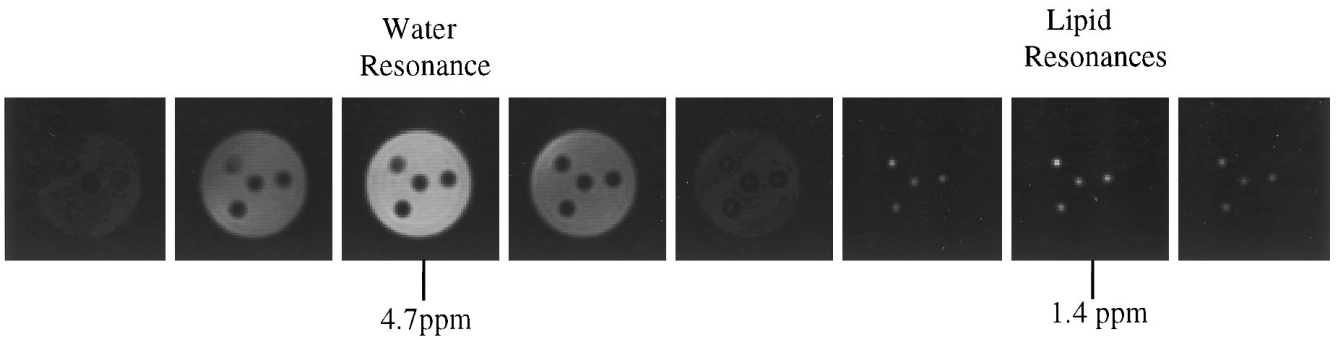

FIG. 11. Spatial–spectral reconstruction of the ^{1}H test phantom. The data were acquired with the GR_{ss} sequence. Each image represents a 83 Hz wide spectral bin of the same axial slice.

In Vivo ^{1}H and ^{23}Na GR_{sp} RFb Imaging of a Human Hand

An axial and coronal slice reconstructed from the time-binned FID ($b = 0$) ^{1}H human hand data are shown in Fig. 14a. The images contain both fat and water which are unresolved. A full spatial/spectral reconstruction was also performed using the *k*-FID/gridding method. Figure 14b shows representative spectra from soft-tissue, bone-marrow, and bone-wall voxels. The soft-tissue and bone-marrow spectra demonstrate enhanced water and lipid lines respectively and the bone-wall voxel spectrum shows reduced total signal intensity. There is no baseline offset evident. Figure 14c shows axial water and lipid slices computed using peak-area calculations. The water image contains signal mostly

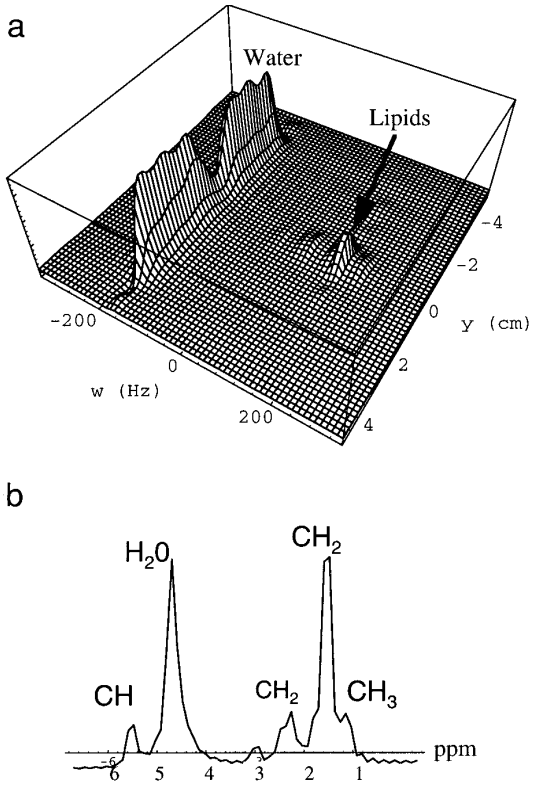

FIG. 12. (a) GR_{sp} data—a spatial/spectral surface plot showing intensity vs chemical shift vs position along the vertical line shown in Fig. 10 for a central slice in *z*. The plot demonstrates the spectral and spatial PSFs. (b) Absorption spectrum from a voxel containing both water and lipid signals.

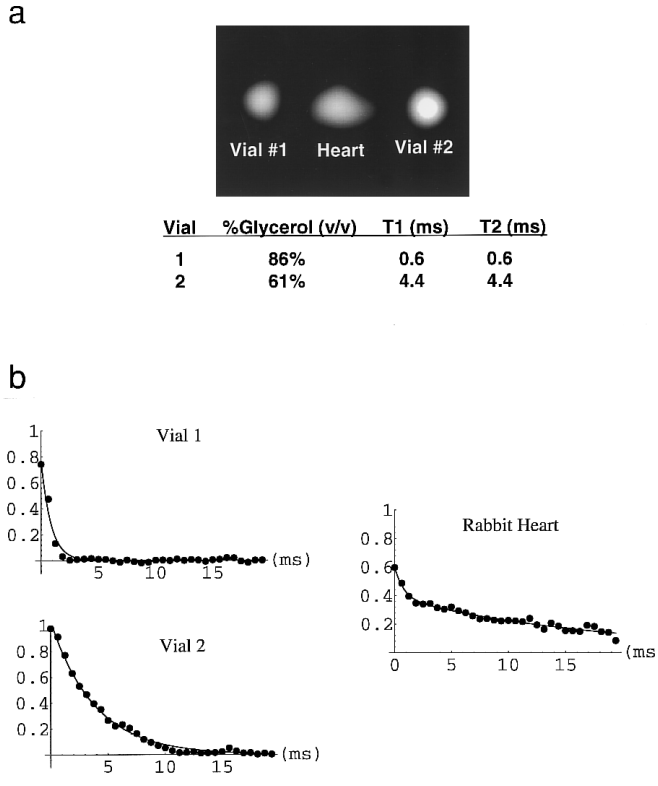

Vial	%Glycerol (v/v)	T1 (ms)	T2 (ms)
1	86%	0.6	0.6
2	61%	4.4	4.4

FIG. 13. (a) *In vitro* ^{23}Na reconstructed time-binned axial slice. The two reference vials as well as the heart are visible. (b) Reconstructed ^{23}Na FIDs from three voxels which were reconstructed with both the *b* and *b′* groupings. The data are displayed in a fashion similar to that of Fig. 6. Vial 1 and vial 2 FIDs were fitted to monoexponential decay curves. The rabbit heart was fitted to a biexponential decay curve. The fitting results are shown in Table 1.

TABLE 1
Intensity and Transverse Relaxation-Time Measurements for ^{23}Na Data (Fig. 13b) Using the *b* Grouping, *b′* Grouping, and *b* and *b′* Groupings Combined

Grouping	Vial 1 (T_2 = 0.64 ms)	Vial 2 (T_2 = 4.4 ms)	Rabbit heart
b	A_f = 0.79 ± 0.00 T_{2_f} = 0.70 ± 0.01	A_s = 1.01 ± 0.00 T_{2_s} = 3.91 ± 0.00	A_f = 0.23 ± 0.00 T_{2_f} = 0.69 ± 0.02 A_s = 0.39 ± 0.00 T_{2_s} = 18.50 ± 0.27
b′	A_f = 1.84 ± 0.04 T_{2_f} = 0.46 ± 0.01	A_s = 1.08 ± 0.00 T_{2_s} = 3.71 ± 0.02	A_f = 0.43 ± 0.25[a] T_{2_f} = 0.47 ± 0.21 A_s = 0.39 ± 0.01 T_{2_s} = 18.33 ± 0.70
Both (*b* + *b′*)	A_f = 0.78 ± 0.03 T_{2_f} = 0.82 ± 0.06	A_s = 1.03 ± 0.01 T_{2_s} = 3.84 ± 0.03	A_f = 0.23 ± 0.01 T_{2_f} = 0.70 ± 0.07 A_s = 0.39 ± 0.00 T_{2_s} = 18.50 ± 0.16

Note. Vial 1 was fitted to a monoexponential curve given by $A_f\exp(-t/T_{2_f})$. Vial 2 was fitted to a monoexponential curve given by $A_s\exp(-t/T_{2_s})$. The rabbit heart voxel was fitted to a biexponential curve.

[a] Nonlinear fitting routine did not converge for rabbit heart voxel using *b′* grouping.

from soft tissue and the lipid image shows high signal from bone marrow and subcutaneous fat.

Figure 15a shows an axial ^{23}Na slice of the hand. Also shown is a coronal projection which was constructed by summing up several reconstructed coronal slices. The SNR of the reconstructed axial slices was approximately 35:1 and spatial resolution was sufficient to visualize the signal void associated with the metacarpals in the axial slice. Figure 15b shows a reconstructed FID from a soft-tissue voxel which has been fitted to a biexponential curve using both the combined *b* and *b′* groupings. The voxel is from a region posterior to and between the second and third metacarpels. A clear multiexponential signal is evident. The fitted values of the short and long transverse relaxation times were 0.90 ± 0.43 and 13 ± 0.24 ms, respectively. The ratio of the short-T_2 to long-T_2 intensity was 0.22 ± 0.02. Although many voxels displayed such biexponential behavior, some voxels were predominantly monoexponential.

DISCUSSION

The experimental results demonstrate that continuously oscillating gradient trajectories can be used to produce 4D spectral/spatial estimates of both long- and short-T_2 species. Because of the steady-state nature of the gradient waveforms, no special B_0 eddy current compensation was required other than gradient-phase calibration.

The AP-SSFP ^{1}H phantom images, which were acquired in 25 s (N_{avg} = 2), displayed an effective isotropic resolution of 4 mm (0.03 cm^3) over a 12.8 cm FOV. With a T_2 of 40 ms and T_R of 10 ms, the maximum theoretical sensitivity increase using the SSFP technique over a spoiled sequence is 70% (Eqs. [30] and [31]) which is quite significant. Because of the short T_R, chemical-shift resolution was sufficient only to separate water and lipid signals. For finer chemical-shift resolution, a longer readout time is required which mandates a longer T_R. Hence, GR_{ss} excitation becomes impractical and GR_{sp} is advised. The experimental ^{1}H phantom results with GR_{sp} show that CH, CH_2, and CH_3 groups were well resolved and the *in vivo* hand images acquired in 144 s (N_{avg} = 2) show well-separated water and lipid signals. These phantom and *in vivo* results suggest that a future application may include ^{23}Na chemical-shift imaging with shift reagents (*50*) which requires the ability to resolve short T_2 signals.

One promising application of imaging with continuously oscillating gradients is relaxographic localization to identify complex transverse relaxation processes such as those exhibited by the ^{23}Na ion. PSF analyses show the ability to separate ''short'' and ''long'' T_2^* signals will depend upon the gradient-oscillation frequency and the subsequent influence of τ upon the spatial PSF. The *in vitro* ^{23}Na spatial–temporal images of the rabbit heart with two reference vials show that, for a practical gradient-oscillation frequency of 800 Hz, short and long T_2 ^{23}Na components may be differentiated. The vial 1 solution was used to simulate an *in vivo* short T_2 component with a value of T_2 = 0.64 ms (τ = 0.5, RFb excitation). Both the *b* grouping and the combined *b* and *b′* groupings yielded similar T_2 estimates which were within 30% of the actual value (Table 1). The signal intensity was underestimated by approximately 20% as is predicted by theory due to the effect of T_2 upon the PSF. The fact that the relaxation rate was relatively well estimated, however, suggests that possible postprocessing algorithms may be de-

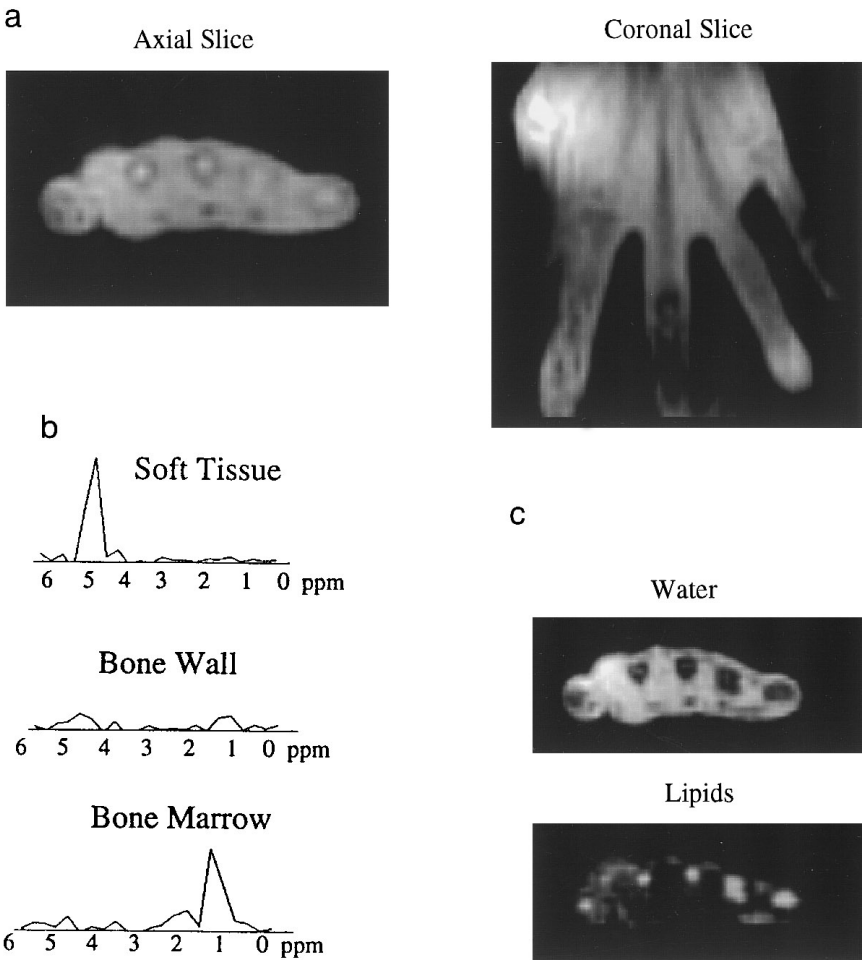

FIG. 14. (a) *In vivo* ^{1}H time-binned ($b = 0$) images of a human hand reconstructed with both axial and coronal orientations. The region of high signal intensity on the left side of the image is due to an inhomogeneity associated with the RF probe. (b) Three characteristic ^{1}H spectra. Differentiation can be made between soft tissue (water), bone wall (reduced signal), and bone marrow (lipid). (c) Computed water and lipid images using peak-area calculations. The water image is composed of mainly soft tissue and the lipid image is predominantly from bone marrow and subcutaneous fat.

veloped to correct for the degraded $b = 0$ PSF. In contrast, using just the b' grouping, the signal intensity was overestimated by more than 85% and may not be possible to predict. Note that, since a full spatial–spectral *k*-FID reconstruction yields a signal characterized by the b' grouping (Eqs. [26], [27]), the time-binning process, which separately reconstructs the $b = 0$ image, appears superior for estimating very short T_2 signal intensities and relaxation rates. All three groupings shown in Table 1 generated good estimates of signal intensities for vial 2 ($T_2 = 4.4$ ms, $\tau = 3.5$). However, the T_2 estimates were slightly low (11–25%), which may be a result of the difference between T_2^* and T_2.

The *in vitro* rabbit heart voxel FID appears multiexponential from visual inspection. For a biexponential fit, both the b grouping and the combined b and b' groupings yielded a 35% fast-relaxing component intensity with a T_2 of approximately 700 μs ($\tau = 0.56$) and a 65% slow-relaxing component with a T_2 of approximately 18.5 ms. More research is required to determine the importance of this information and its correlation with ischemia. However, the results are consistent with data from nonlocalized FIDs (*51*). The *in vivo* data from the human hand were also fitted to a biexponential curve with little fitting error. Although two distinct values of T_2 were identified, the gradient-oscillation frequency (500 Hz) may have been too small to accurately estimate the intensity and time constant of the short component ($\tau_f = 0.45 \pm 0.21$) due to PSF broadening.

In evaluating the imaging schemes in general, it is important to compare both the RF excitation options as well as the gradient trajectories. As shown under Theory, the two excitation sequences (RFa and RFb) force different *k*-space sampling-density functions which can impact both the SNR and the PSF shape. With excitation at a gradient maximum (RFa), the *k*-space weighting tends to be more uniform and can yield a small ($\approx$20%) reduced theoretical noise variance compared with excitation at a gradient zero (RFb). In addi-

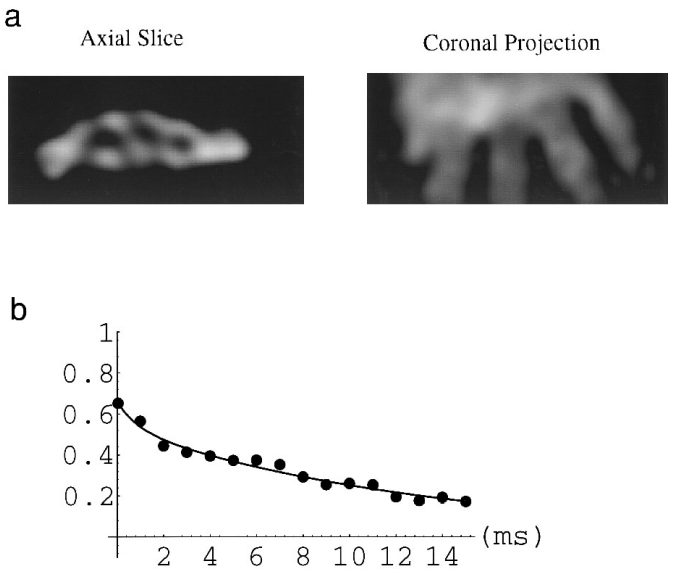

FIG. 15. *In vivo* ^{23}Na data from a human hand. (a) Axial slice showing sufficient resolution to view the void associated with the metacarpels. A reconstructed coronal 2D projection of the hand is also shown. (b) Voxel FID from between the second and third metacarpals which has been fitted to a biexponential curve using the b and b' groupings combined. The fit is given by $\hat{s}(t) = (0.12 \pm 0.01)\exp[t/(0.90 \pm 0.43)] + (0.54 \pm 0.01)\exp[t/(13 \pm 0.24)]$, where the relaxation times are measured in milliseconds. The intensity values are in arbitrary units and show relative strengths of the short- and long-T_2 signals.

tion, the time-binned RFa PSF will, in some instances, be less corrupted by B_0 inhomogeneities and T_2 effects. Another advantage of the RFa sequence is that both sides of the k-space origin are sampled after each excitation, thus providing improved sampling efficiency. However, this RFa implementation requires twice as much gradient magnitude and slew rate capability to attain an equivalent maximum radius in k-space (Eqs. [3], [4]).

Experimentally, the RFb excitation sequence appears more practical to implement. This is partly because the maximum pulse bandwidth that is necessary to excite the entire sample is lower. Hence, the RF pulse may be longer, thereby reducing peak power requirements or allowing for larger flip angles to improve the SNR. For our implementations, 100 μs pulse duration times could be used for RFb excitation while the RFa excitation time was approximately 20 μs. Even in this case, with RFa, crucial points near the k-space origin could not be sampled. Another advantage of RFb excitation is that the pulse may be placed slightly before the gradient zero to allow for probe ringdown before sampling the k-space origin.

In comparing the two gradient trajectories (GR_{ss} and GR_{sp}), several factors must be considered. These include contrast, sensitivity, immunity to artifacts, and ease of implementation. Depending upon T_R and T_2, the sensitivity increase afforded by the steady-state sequence (GR_{ss}) can be quite significant. Moreover, contrast tends to behave as the ratio of T_2/T_1 which may be desirable for proton density imaging. GR_{ss} may also offer a quicker imaging time than GR_{sp} since a spoiler gradient is not required and the gradient steady-state condition is not destroyed and restarted between successive RF excitations. The problem with implementing GR_{ss} results from the tight restrictions placed upon B_0 homogeneity that are necessary to maintain the B_0-uniform-field condition. Slight dephasing caused by eddy currents, motion, or flow in the presence of a gradient can upset the steady-state condition. In addition, the SSFP equations are not necessarily valid for a spin-$\frac{3}{2}$ system such as ^{23}Na as higher-order coherences may be created (*52*). In comparison, because a spoiler gradient is applied, GR_{sp} is immune to many of the implementation problems and artifacts associated with GR_{ss}. However, depending upon the excitation parameters and relaxation rates, GR_{sp} may tend to be more T_1 weighted which can impact upon the ability to quantify spin densities.

CONCLUSION

The feasibility of rapid 4D imaging of short-T_2 species using continuously oscillating gradients has been demonstrated. The next stages of development will require both clinical and technical investigations. For example, for ^{23}Na relaxography, relaxation-time and signal-intensity measurements must be correlated with pathology while the problem of $b = 0$ PSF blurring may need to be addressed via correction algorithms and/or increased gradient-oscillation frequencies. A key feature of the techniques proposed is that a variety of RF excitation and k-space sampling options exist which should allow for flexibility in optimizing specific scanning parameters for different targeted applications. Ultimately, such applications may include water/lipid chemical-shift imaging and ^{23}Na chemical-shift imaging with shift reagents, as well as ^{23}Na relaxographic imaging.

APPENDIX

The FID ($b = 0$) RFa spatial PSF is derived by substituting the received k-domain signal given by Eq. [12] into Eq. [10]. After this substitution, the RFa PSF, written as function of r and T_2^*, is

$$\mathrm{PSF}_{\mathrm{RFa}}(r, T_2^*) = \frac{3}{k_{\max}^3} \times \int_0^{k_{\max}} \exp\left[-\frac{1}{T_2^* \Omega_0} \sin^{-1}\left(\frac{k_r}{k_{\max}}\right)\right] \mathrm{sinc}(2rk_r) k_r^2 dk_r. \quad [A1]$$

Introducing a dimensionless constant $\tau = T_2^* f_0$, which relates the transverse relaxation time to the gradient-oscilla-

tion frequency $f_0 = \Omega_0/(2\pi)$ (Hz), Eq. [A1] can be simplified by substituting $\sin(k') = k_r/k_{max}$ and $a = 1/(2\pi\tau)$:

$$\mathrm{PSF}_{\mathrm{RFa}}(r, a) = \frac{3}{2\pi k_{max}} \times \int_0^{\pi/2} e^{-ak'} \sin[2\pi r k_{max} \sin(k')] \sin(k') \cos(k') dk'. \quad [A2]$$

Using the identity

$$e^{iA \sin(k_r)} = \sum_{n=-\infty}^{\infty} J_n(A) e^{ink_r}, \quad [A3]$$

Eq. [A2] may be written as

$$\mathrm{PSF}_{\mathrm{RFa}}(r, a) = 3 \sum_{m=-\infty}^{\infty} \frac{J_m(2\pi r k_{max})}{2\pi r k_{max}} \int_0^{\pi/2} e^{-ak'} \sin(mk') \sin(k') \cos(k') dk',$$

$$= \frac{3}{\pi r k_{max}} \sum_{m=1,3,5,\ldots}^{\infty} J_m(\pi r k_{max}) \frac{2ma + e^{-a\pi/2}(-1)^{(m-1)/2} \times (4 + a^2 - m^2)}{16 + 8a^2 + a^4 - 8m^2 + 2a^2m^2 + m^4}. \quad [A4]$$

The resulting point-spread function, $\mathrm{PSF}_{\mathrm{RFa}}(r, a)$, is a series of odd-order Bessel functions of the first kind which decreases as $1/m^2$.

The $b = 0$ RFb spatial PSF is derived by substituting the received k-domain signal given by Eq. [14] into Eq. [10]. Substituting $a = 1/(2\pi\tau)$ and $\sin(k') = k_r/k_{max}$ and using Eq. [A3], the point-spread function, $\mathrm{PSF}_{\mathrm{RFb}}(r, a)$, is calculated to be the summation of even- and odd-order Bessel functions,

$$\mathrm{PSF}_{\mathrm{RFb}}(r, a) = \sin(k_{max} r) \times [J_0(\pi k_{max} r) + 2 \sum_{m=2,4,6,\ldots}^{\infty} \beta(a, m) J_m(\pi k_{max} r)] - 2\cos(k_{max} r) \sum_{m=1,3,5,\ldots}^{\infty} \beta(a, m) J_m(\pi k_{max} r), \quad [A5]$$

where

$$\beta(a, m) = \left(\frac{3}{8\pi r k_{max}}\right) \times \left\{ \frac{e^{-a\pi}[(4 - a^2 - m^2)(-1)^m - 1]}{16 + 8a^2 + a^4 - 8m^2 + 2a^2m^2 + m^4} + \frac{e^{-a\pi}[(1 + a^2 - m^2)(-1)^m + 1]}{1 + 2a^2 + a^4 - 2m^2 + 2a^2m^2 + m^4} \right\}.$$

ACKNOWLEDGMENTS

The authors thank Dr. Blaise Frederick, Dr. Sundar Armatur, and Dr. K. T. Brennan for many helpful discussions. The work was supported in part by a National Science Foundation Graduate Scholarship and in part by U.S. Department of Health and Human Services under Grant HI25840-12A1.

REFERENCES

1. A. Macovski, *Magn. Reson. Med.* **2,** 29–40 (1985).
2. I. Shenberg and A. Macovski, *IEEE Trans. Med. Imaging* **4,** 144–152 (1985).
3. I. Shenberg and A. Macovski, *IEEE Trans. Med. Imaging* **4,** 165–174 (1985).
4. I. Shenberg and A. Macovski, *IEEE Trans. Med. Imaging* **5,** 121–127 (1986).
5. I. Shenberg and A. Macovski, *Med. Phys.* **13,** 164–169 (1986).
6. S. J. Norton, *IEEE Trans. Med. Imaging* **6,** 21–31 (1987).
7. S. D. Rand and A. Macovski, *IEEE Trans. Med. Imaging* **6,** 346–355 (1987).
8. P. J. McDonald and P. F. Tokarczuk, *J. Phys. E. Sci. Instrum.* **22,** 948–951 (1989).
9. Y. M. Daud and M. R. Halse, *Physica B* **176,** 167–172 (1992).
10. D. Burstein and E. T. Fossel, *Magn. Reson. Med.* **4,** 261–273 (1987).
11. W. Perman, D. Thomasson, M. Bernstein, and P. Turski, *Magn. Reson. Med.* **9,** 153–169 (1989).
12. J. B. Ra, S. K. Hilal, and C. H. Oh, *J. Comput. Assist. Tomogr.* **13,** 302 (1989).
13. S. J. Kohler, N. H. Kolodny, D. J. D'Amico, S. Balasubramaniam, P. Mainardi, and E. S. Gragoudas, *J. Magn. Reson.* **82,** 505–517 (1989).
14. Y. Boulanger and P. Vinay, *Can. J. Physiol. Pharmacol.* **67,** 820–828 (1989).
15. J. H. Lee, C. Labadie, and C. S. Springer, Abstracts of the Society of Magnetic Resonance in Medicine, 11th Annual Meeting, p. 2214, 1992.
16. J. H. Lee, Y. Seo, M. Murakami, C. Labadie, and C. S. Springer, Abstracts of the Society of Magnetic Resonance in Medicine, 11th Annual Meeting, p. 2222, 1992.
17. G. Gold, J. Pauly, G. Glover, J. Moretto, A. Macovski, and R. Herfkens, *J. Magn. Reson. Imaging* **3,** 399–407 (1993).
18. G. Gold, J. Pauly, A. Macovski, and R. Herfkens, *Magn. Reson. Med.* **34,** 647–654 (1995).
19. P. Mansfield, *Magn. Reson. Med.* **1,** 370–386 (1984).
20. S. T. S. Wong and M. S. Roos, *Magn. Reson. Med.,* **32,** 778–784 (1994).
21. G. H. Glover, J. M. Pauly, and K. M. Bradshaw, *J. Magn. Reson. Imaging* **2,** 47–52 (1992).
22. J. D. O'Sullivan, *IEEE Trans. Med. Imaging* **4,** 200–207 (1985).
23. J. I. Jackson, C. H. Meyer, D. G. Nishimura, and A. Macovski, *IEEE Trans. Med. Imaging* **10,** 473–478 (1991).
24. C. E. Metz and K. Doi, *Phys. Med. Biol.* **24,** 1079–1106 (1979).
25. A. Macovski, ''Medical Imaging Systems,'' Prentice–Hall, Englewood Cliffs, New Jersey, 1983.
26. A. Maeda, K. Sano, and T. Yokoyama, *IEEE Trans. Med. Imaging* **7,** 26–31 (1988).
27. D. Noll, J. Pauly, C. Meyer, D. Nishimura, and A. Macovski, *Magn. Reson. Med.* **25,** 319–333 (1992).

28. E. W. McFarland, *Magn. Reson. Imaging* **10,** 269–278 (1992).

29. R. N. Bracewell, ''The Fourier Transform and Its Applications,'' McGraw–Hill, New York, 1978.

30. A. V. Oppenheim and R. W. Schafer, ''Discrete-Time Signal Processing,'' Prentice–Hall, Englewood Cliffs, New Jersey, 1989.

31. D. B. Twieg, J. Katz, and R. M. Peshock, *J. Magn. Reson.* **5,** 32–46 (1987).

32. A. Zakhor, R. Weisskoff, R. Rzedzian, *IEEE Trans. Signal Process.* **39,** 2056–2065 (1991).

33. K. M. Hanson, *Med. Phys.* **6,** 441–451 (1979).

34. D. B. Twieg, *Med. Phys.* **10,** 610–621 (1983).

35. A. A. Maudsley, S. K. Hilal, W. H. Perman, and H. E. Simon, *J. Magn. Reson.* **51,** 147–152 (1983).

36. D. B. Twieg, *Magn. Reson. Med.* **2,** 437–452 (1985).

37. R. R. Ernst and W. A. Anderson, *Rev. Sci. Instrum.* **37,** 93–102 (1966).

38. R. Freeman and H. D. W. Hill, *J. Magn. Reson.* **4,** 366–383 (1971).

39. L. Darasse, L. Mao, and H. Saint-James, Abstracts of the Society of Magnetic Resonance in Medicine, 5th Annual Meeting, p. 944, 1986.

40. J. A. Utz, R. J. Herfkins, C. D. Johnson, A. Shimakawa, N. Pelc, G. Glover, G. A. Johnson, and C. E. Spritzer, *Am. J. Roentgenol.* **148**(3), 629–633 (1987).

41. H. Weber, D. Purdy, M. Deiming, and A. Oppelt, Abstracts of the Society of Magnetic Resonance in Medicine, 5th Annual Meeting, p. 957, 1986.

42. Y. Zur, S. Stokar, and P. Bendel, *Magn. Reson. Med.* **6,** 175–193 (1988).

43. K. Sekihara, *IEEE Trans. Med. Imaging* **6,** 157–164 (1987).

44. Y. Zur, M. L. Wood, and L. J. Neuringer, *Magn. Reson. Med.* **21,** 251–263 (1991).

45. A. Haase, J. Frahm, D. Matthaei, W. Hanicke, and K.-D. Merboldt, *J. Magn. Reson.* **67,** 258–266 (1986).

46. J. W. Carlson, K. A. Derby, K. C. Hawryszko, and M. Weideman, *Magn. Reson. Med.* **26,** 191–206 (1992).

47. J. Murphy-Boesch, R. Srinivasan, L. Carvajal, and T. R. Brown, *J. Magn. Reson. B* **103,** 103–114 (1994).

48. B. deB. Frederick, M. S. Roos, and S. T. S. Wong, Abstracts of the Society of Magnetic Resonance in Medicine, 10th Annual Meeting, p. 726, 1991.

49. W. H. Press, B. P. Flannery, S. A. Teukolsky, and W. T. Vetterling, ''Numerical Recipes in C: The Art of Scientific Computing,'' Cambridge Univ. Press, New York, 1988.

50. R. K. Gupta and P. Gupta, *J. Magn. Reson.* **47,** 344–350 (1982).

51. S. Armatur, personal communication, 1996.

52. J. Pekar and J. S. Leigh, *J. Magn. Reson.* **69,** 582–584 (1986).